Supporting Information

Molecular layer deposition of zeolitic imidazolate framework-8 films

Jorid Smets,[a,b,‡] Alexander John Cruz,[a,c,d,‡,†] Víctor Rubio-Giménez,[a] Max L. Tietze,[a] Dmitry E. Kravchenko,[a] Giel Arnauts,[a] Aleksander Matavž,[a] Nathalie Wauteraerts,[a] Min Tu,[a,§] Kristof Marcoen,[c] Inhar Imaz,[e] Daniel Maspoch,[e,g] Maxim Korytov,[d] Philippe M. Vereecken,[a,d] Steven De Feyter,[f] Tom Hauffman,[c] and Rob Ameloot[a,*]

[a] Center for Membrane Separations, Adsorption, Catalysis, and Spectroscopy (cMACS), KU Leuven - University of Leuven, Celestijnenlaan 200F, Leuven, 3001, Belgium

[b] Sustainable Energy, Air & Water Technology (DuEL), Department of Bioscience Engineering, University of Antwerp, Groenenborgerlaan 171, 2020 Antwerp, Belgium

[c] Research Group of Electrochemical and Surface Engineering, Department of Materials and Chemistry, Vrije Universiteit Brussel, Pleinlaan 2, Brussels, 1050, Belgium

[d] Imec, Kapeldreef 75, Leuven, 3001, Belgium

[e] Catalan Institute of Nanoscience and Nanotechnology (ICN2), CSIC and The Barcelona Institute of Science and Technology, Campus UAB, Bellaterra, 08193 Barcelona, Spain

[f] Department of Chemistry, Division of Molecular Imaging and Photonics, KU Leuven, Leuven, Belgium

[g] ICREA Pg. LluísCompanys 23, 08010 Barcelona, Spain

‡ These authors contributed equally.

† Baker Hughes, Schumanplein 6, Brussels 1040 Belgium

§ 2020 X-Lab and State Key Laboratory of Transducer Technology, Shanghai Institute of Microsystem and Information Technology, Chinese Academy of Sciences, Shanghai 200050, China

E-mail: rob.ameloot@kuleuven.be

Table of Contents

Supporting Information

Methods

Substrates: Device grade, p-type, 200 mm Si wafers (Si-Mat, resistivity = 1-30 Ω cm, thickness = 725 ± 25 µm) were used and smaller pieces were cleaved.

Solution-deposited films: ZIF-8 thin films were synthesized using a previously described deposition route by Lu and Hupp.[1] In short, a silicon substrate was first cleaned in piranha solution and extensively washed with deionized water and methanol. Then, the substrate was immersed in the mixture of 2-methylimidazole (50 mM; Sigma Aldrich, 99%) and zinc nitrate hexahydrate (25 mM; Alfa Aesar, 99%) solutions for 30 min. The deposition step was repeated several times to adjust the final film thickness. After the last layer deposition, the sample was washed 3 times in methanol and once in ethanol, and dried under nitrogen flow.

ZIF-8 MOF-CVD: Chemical vapor deposition of ZIF-8 was performed in the same ALD reactor used for ZIF-8 MLD (Savannah S-200 thermal ALD reactor, Veeco Instruments Inc.). The used process was according to our previous work.[2] The ZIF-8 CVD process employs deionized water (DIW), diethylzinc (DEZ, 97%, STREM), and freshly-ground HmIM (30 g, 99%, Sigma Aldrich) as precursors. Nitrogen (99.999%) was the carrier and purging gas used and sourced from a cleanroom header. First, 3 nm of zinc oxide is deposited by supplying alternating pulses (0.015 s) of DEZ and water, separated by N_2 purges (5 s). Afterward, the HmIM bubbler is heated and purged as described in the ZIF-8 MOF-MLD section. HmIM is bubbled to the reactor chamber in stopped-flow conditions until the ellipsometry profile of the monitoring substrate (Si wafer) is constant.

Ellipsometry during deposition: The optical properties of the deposited layers were measured during deposition using an M-2000x spectroscopic ellipsometer (J. A. Woollam Co. Inc., λ = 246-1000 nm), using a lid with fused silica viewports. The optical parameters of the layer were fit with an extended Cauchy model at the end of the deposition, these parameters are fixed while the thickness is calculated as a function of deposition time.

Cauchy equation: $\qquad\qquad n(\lambda) = A + \frac{B}{\lambda^2} + \frac{C}{\lambda^4}$

Urbach equation: $\qquad\qquad k(\lambda) = A_k e^{B_k(E-E_b)}$ $\qquad\qquad$ if $k \neq 0$

Full-wafer thickness mapping: The thickness and refractive index (λ = 633 nm) of the ZIF-8 layers deposited on 200 mm wafers were measured with a KLA-Tencor ASET F5x thin film measurement system equipped with a motorized stage. A radial map of Psi and Delta (λ = 400-800 nm) was recorded for 100 points evenly distributed over the wafer.

Ellipsometric porosimetry: Known concentrations of methanol vapor in N_2 flow (420 s, 550 sccm) were generated by a home-built vapor dosing system and were alternated by N_2 purges (180 s, 550 sccm). The uptake of a film can be approximated by:[3]

$$\tau = \frac{l^2}{3D}$$

With τ the time constant, l the thickness of the MOF layer, and D the transport diffusion coefficient (from Chmelik *et al.*[4], 1e-12 m^2/s). The time constant for methanol diffusion in a 30 nm MOF film therefore is 3e-4 s. At 3τ, 95% of the pores will be filled, *i.e.*, after 9e-4 s. Thus the methanol exposure and purge times are sufficiently long to overcome diffusion limitations. The dosing experiment is plotted in **Figure S22** as a function of time and the points at which data for the isotherm graphs are exported are indicated in red.

The sample (30 cycles of ZIF-8 MLD) was situated in an environmental cell with fused silica viewports. The optical constants of the material were determined by ellipsometry with a Woollam iSE ellipsometer. For direct ZIF-8 MLD, the layer was modeled as an extended Cauchy layer. Afterward, all optical parameters and thickness were fixed except for A and B, these two values

were fitted as a function of methanol vapor concentration, from which the refractive index at each point can be calculated. For two-step ZIF-8 MLD an effective medium approximation (Bruggemann) model was used to account for the partial surface coverage, combining a Cauchy model with a fitted void fraction (often about 10 vol%).[5]

$$f_{MOF} \frac{\tilde{\varepsilon}_{MOF} - \tilde{\varepsilon}_{EMA}}{\tilde{\varepsilon}_{MOF} + 2\tilde{\varepsilon}_{EMA}} + f_{void} \frac{\tilde{\varepsilon}_{void} - \tilde{\varepsilon}_{EMA}}{\tilde{\varepsilon}_{void} + 2\tilde{\varepsilon}_{EMA}} = 0$$

With $\tilde{\varepsilon}$ the effective complex dielectric function, and f the volume fraction of each constituent.

When the void fraction is not included in the modelling, a lower refractive index is modeled (n = 1.21).

Atomic Force Microscopy (AFM): Topography images were recorded in intermittent contact mode using an NX-Hivac (Park Systems) under Ar atmosphere, an Agilent AFM 5100, and a Bruker multimode 8 setup under ambient conditions using Pt/Ir cantilevers for the first system and Si cantilevers (AC160TS-R3, Olympus Corporation) for the two other ones. Data analysis was performed using WSXM 5.0 software.[6]

Grazing incidence and specular X-ray diffraction (GIXRD and sXRD): Diffraction patterns were recorded using a Malvern PANalytical Empyrean diffractometer equipped with a Cu anode operating at 45 kV and 40 mA and PIXcel3D solid-state detector. Thin film samples were placed on a flat stage and measured in scanning line mode with a step size of 0.053° and a counting time of 1000 s per step. On the incident beam side, a 1/32° fixed anti-scatter slit was used to limit the divergence of the beam. Additionally, a 1/8° divergence slit and a 4 mm beam mask were used. At the secondary side, a 1/8° anti-scatter slit together with a 0.04 Soller slit were used. For GIXRD measurements an incident beam angle of 0.2° was used.

Synchrotron GIXRD: Measurements were carried out at the BL9 beamline of DELTA synchrotron (λ = 1.03 Å; Dortmund, Germany)[7] and the XRD1 beamline of the Elettra Synchrotron (λ = 1.4 Å; Trieste, Italy) using a stationary MAR or Pilatus 2M detector, respectively. Thin film samples were placed on sample holders mounted on multi-axis diffractometers at distances of approximately 350 and 200 mm, respectively (both calibrated with LaB_6 reference samples). Multiple pixel images were acquired at various angles of incidence and then further processed into diffractograms and reciprocal space maps using FIT2D[8] and GIDVis[9] software packages. All integrated diffractograms were converted from Q to 2θ using CuKα wavelength 1.54 Å.

Hard X-ray photoelectron spectroscopy (HAXPES): Hard X-ray photoemission spectroscopy measurements were performed at IMO-IMOMEC (Hasselt University, Belgium) with a HAXPES lab system (Scienta Omicron, Sweden, Germany) equipped with a liquid gallium jet source (Excillum MetalJet D2; Excillum, Sweden) and a monochromator (HAX9-5; Scienta Omicron) for generating a monochromized (420 meV) Ga Kα beam of hν = 9251.6 eV. A 200 mm hemispherical analyzer (R4000, Scienta Omicron) combined with a 40 mm microchannel plate/charge-coupled device detector (MCP/CCD, VG Scienta) with 435 channels was used for photoelectron detection. A slit of 1.0 mm and pass energies of 500 and 200 eV were used for survey and core-level scans, respectively. For the latter, this configuration yields an energy resolution of 660 meV. To verify the correct energy calibration of the instrument under Ga Kα, Au 4f core level scans on a gold reference foil were performed. The hard X-ray beam exiting the monochromator and the analyzer is aligned under a right angle while the sample is tilted by ca. 3° w.r.t. to the incident X-ray beam. Before the measurements, the samples were stored in nitrogen. To estimate atomic ratios, recently published theoretical elemental photoemission cross sections for Ga Kα excitation were used, as in our previous work on ZIF-8 CVD films.[10,11]

Conductive (c-)AFM: A Bruker's Dimension Icon AFM system was used to check for pinholes in films on Si substrates. The samples were electrically contacted with Ag paint using a custom sample holder. A heavily doped full diamond tip was used to test the samples with an applied DC bias voltage of 8.0 V at a scan speed of 0.5 Hz. The threshold bias voltage for the direct ZIF-8 MLD coating was determined to be > 5.0 V. All c-AFM measurements were carried out in a glove box under an Ar atmosphere.

Synthesis and formation of ZIF-8 and ZIF-67 supercrystals: $Zn(OAc)_2 \cdot 2H_2O$ (99%) [for ZIF-8] and $Co(Ac)_2.4H_2O$ (99%) [for ZIF-67] in DI water were separately added into HmIM (95%) and cetyltrimethylammonium bromide (99%) solutions. The mixture was stirred and left for 2 h to form the ZIF crystals. After washing, the crystals were suspended in water and dropcasted on Si substrates. The coated substrates were dried and activated in an oven at 120 °C.[12]

Electron microscopy: Scanning electron microscopy (SEM) images were collected using a Philips XL30 FEG and a JEOL JSM 6010-LV. Before imaging, the samples were coated with 3-5 nm of Pt.

Infrared spectroscopy (IR): A Varian 670 Fourier Transform-IR spectrometer with an actively cooled mercury cadmium telluride detector and a Ge crystal plate in the Veemax III module was used for all measurements. For films on Si, the system was used in attenuated total internal reflection configuration; for powders, a Varian 620 FTIR imaging microscope with a slide-on Ge ATR tip was employed.

Thermogravimetric Analysis (TGA): TGA for vapor pressure determination of the HmIM linker was carried out in a Netzsch STA 449 F3 Jupiter TG analyzer under vacuum (2×10^{-2} mbar). The sample was placed in a Knudsen cell with a 122 μm orifice in the lid. The vapor pressure was calculated from the mass loss rate at the isothermal segments according to the Knudsen cell effusion equation.[13] The calculations for the estimation of the vapor pressure curves are detailed below. The same apparatus was used for the characterization of the ZIF-67 crystals.

Table S1 | Summary of some of the reported vapor-phase processes for the layer-by-layer deposition of MOFs and non-porous coordination polymers.

References	Material	Precursors		Activation protocol/ treatments*	Dep. temp. [°C]	Film thickness monitoring	GPC [nm]	Porosity assessment
Salmi, et al.[14]	MOF-5	ZnAc$_2$	1,4-BDC	RH (60%) 24 h DMF, 150 °C, 2 h autoclave	225, 350	*ex situ:* reflectance (optical)	0.65	IPA uptake: micro- and mesoporosity
Salmi, et al.[15]	IRMOF-8	ZnAc$_2$	2,6-NDC	RH (70%) 24 h DMF, 150 °C, 2 h autoclave	260, 300	*ex situ:* reflectance SEM-EDS	0.49	Pd loading and EDS mapping
Ahvenniemi and Karppinen[16]	Cu-terephtalate	Cu(thd)$_2$	TPA	n/a	180, 280	*ex situ:* XRR	0.75	H$_2$O uptake
Multia, et al.[17]	Cu-terephtalate	Cu(thd)$_2$	TPA	2 h @150°C for Kr ads., @40°C for MeOH ads.	180, 220	*ex situ:* XRR	0.22	Kr, MeOH uptake
Medishetty, Devi, et al.[18]	Zn-di-carboxylate- Zn-pyrazolate-carboxylate	(DMA)$_2$ [Zn$_3$(BDC)$_4$] Zn$_4$O (dmcapz)$_6$	TPA	closed-cell heat treatment at 120 °C, 24 h	170, 240, 120	*ex situ:* ellipsometry and SEM	n/a	n/a
Ahvenniemi and Karppinen[19]	Ca-TPA	Ca(thd)$_2$	TPA	n/a	190, 420	*ex situ:* XRR	0.34	n/a
Lausund and Nilsen[20]	UiO-66	ZrCl$_4$	1,4-BDC	acetic acid modulation, 160 °C autoclave	235, 390	*in situ:* QCM	0.7	QCM H$_2$O uptake (~1.9 wt %)
Lausund, Nilsen, et al.[21]	amino func. UiO-66	ZrCl$_4$	2-amino-1,4 BDC	acetic acid modulation, 160 °C autoclave	240, 390	*in situ:* QCM	1	QCM H$_2$O uptake
Lausund, Nilsen, et al.[22]	UiO-66 with bi-aromatic linkers	ZrCl$_4$	NDC BPDC	acetic acid modulation, 160 °C autoclave	260, 390	*in situ:* QCM	0.5-1.5	QCM H$_2$O uptake
Tanskanen and Karppinen[23]	Fe-terephthalate	FeCl$_3$	TPA	n/a	240, 260	*ex situ:* XRR	1.1	n/a
Han et al.[24]	HKUST-1	Cu	BTC	annealing under H$_2$O and O$_2$ exposure	50	*ex situ:* AFM	n/a	H$_2$O uptake
Khayyami et al.[25]	Fe-azobenzene	FeCl$_3$	azo BDC	n/a	250, 290	*ex situ:* XRR	2.5	H$_2$O uptake
Silva et al.[26]	Eu-bearing UiO-66	Eu(thd)$_3$	NH$_2$TA	n/a	180	*ex situ:* SEM	1.4	n/a

MOF-5 = Zn$_4$O(BDC)$_3$; **ZnAc$_2$** = Zn acetate; **BDC** = benzene-1,4-dicarboxylate; **IPA** = isopropyl alcohol; **IRMOF-8** = [Zn$_4$O(NDC)]$_3$; **RH** = relative humidity; **NDC** = naphthalene-2,6-dicarboxylate; **BPDC** = biphenyl-4,40-dicarboxylic acid; **TP(A)** = terephthalic (acid); **thd** = 2,2,6,6-tetramethyl-3,5-heptanedione; **DMA** = dimethylammonium; **DMF** = dimethylformamide; **dmcapz** = 3,5-dimethyl-4-carboxypyrazole; **UiO-66** = [Zr$_6$O$_4$(OH)$_4$][BDC]$_6$; **HKUST-1** = [Cu$_3$(OH$_2$)$_3$(BTC)$_2$], **BTC** = benzene-1,3,5-tricarboxylic acid; **Eu(thd)$_3$** = europium(III)-tris-(2,2,6,6-tetramethyl-3,5-heptanedionate); **NH$_2$TA** = 2-aminoterephthalic acid; **H.P.** = high pressure; **Dep. Temp.** = deposition temperature; **GPC** = growth per cycle; **XRR** = X-ray reflectivity; **AFM** = atomic force microscopy; **QCM** = quartz crystal microbalance; **SEM** = scanning electron microscopy; **EDS** = energy-dispersive X-ray spectroscopy. | *post treatments of non-crystalline, as-deposited layers.
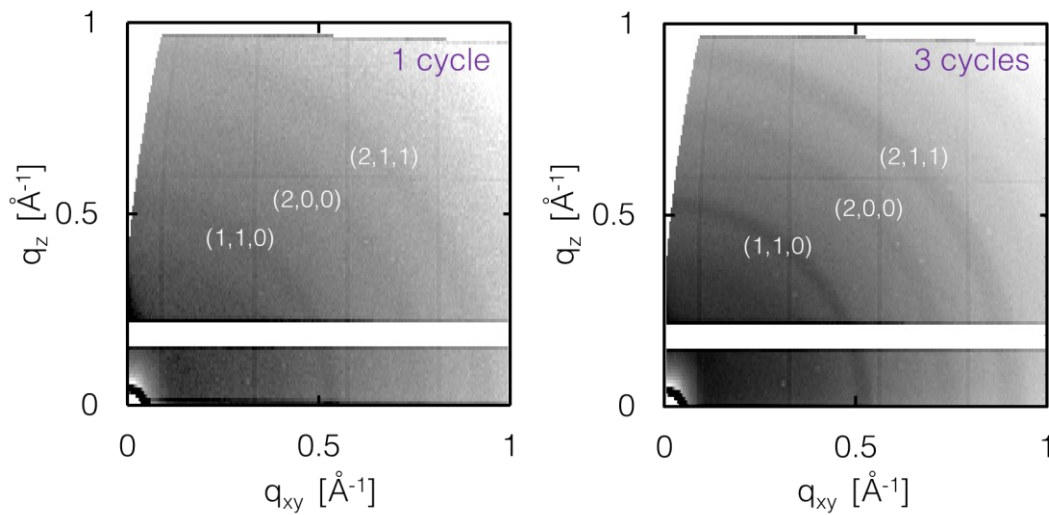
Figure S1 | Synchrotron GIXRD reciprocal space maps of direct ZIF-8 MLD showing crystallinity even at a very low number of cycles.

Vapor pressure determination of 2-methylimidazole (HmIM) *via* thermogravimetry: Knudsen effusion method

Using the Knudsen effusion method, the vapor pressure of HmIM was experimentally determined. With this method, the vapor pressure of the MOF-MLD linker is correlated to the weight loss at several temperature steps. The data collected is modeled with an empirical equation for the steady-state effusion of dilute gases.[27,28] This protocol has been previously demonstrated in various ALD precursors.[29]

The measurements were carried out under dynamic vacuum conditions using an inert process gas. The rate of mass loss ($\frac{dm}{dt}$) at a particular temperature was calculated (**Eqn. 1**) for a particular operating range and fed into the Knudsen equation.[30] The series of vapor measurements can then be fitted using the reduced Clausius-Clapeyron-derived equation (**Eqn. 2**), assuming that the ideal gas law is valid and the latent heat of vaporization is independent of the temperature.

$$P_{sat} = \frac{dm}{dt}\frac{\sqrt{\frac{2\pi RT}{M}}}{AK_c} \qquad [\text{Pa}] \qquad \text{vapor pressure at temperature, T [K]} \qquad \textit{Eqn. 1}$$

$$A = \pi r^2 \qquad [\text{m}^2] \qquad \text{area of the Knudsen cell orifice}$$

$$M \qquad [\text{g mol}^{-1}] \qquad \text{molecular weight of the linker}$$

$$\frac{dm}{dt} \qquad [\text{kg s}^{-1}] \qquad \text{rate of change of mass at temperature, T [K]}$$

$$K_c = \frac{1}{1+\frac{3l}{8r}} \qquad \text{Clausing coefficient}^{a),b)}$$

l = 0.0003   [m]   length of the Knudsen cell orifice

r = 4.86 × 10^6 [m]   radius of the Knudsen cell orifice

[a] a simplified multiplying factor to take into account the resistance of the membrane (orifice) to effusion due to its definite thickness.

[b] this simplification of the Clausing coefficient is valid for experimental conditions where the Knudsen number (ratio of the mean free path to the orifice diameter) is ≥ 10, which is applicable in our process implemented in this work.[31]

$$\ln P = A + \frac{B}{T[K]}$$

Eqn. 2

The data is found to be in agreement with the reported values (**Figure S2**).[32,33]
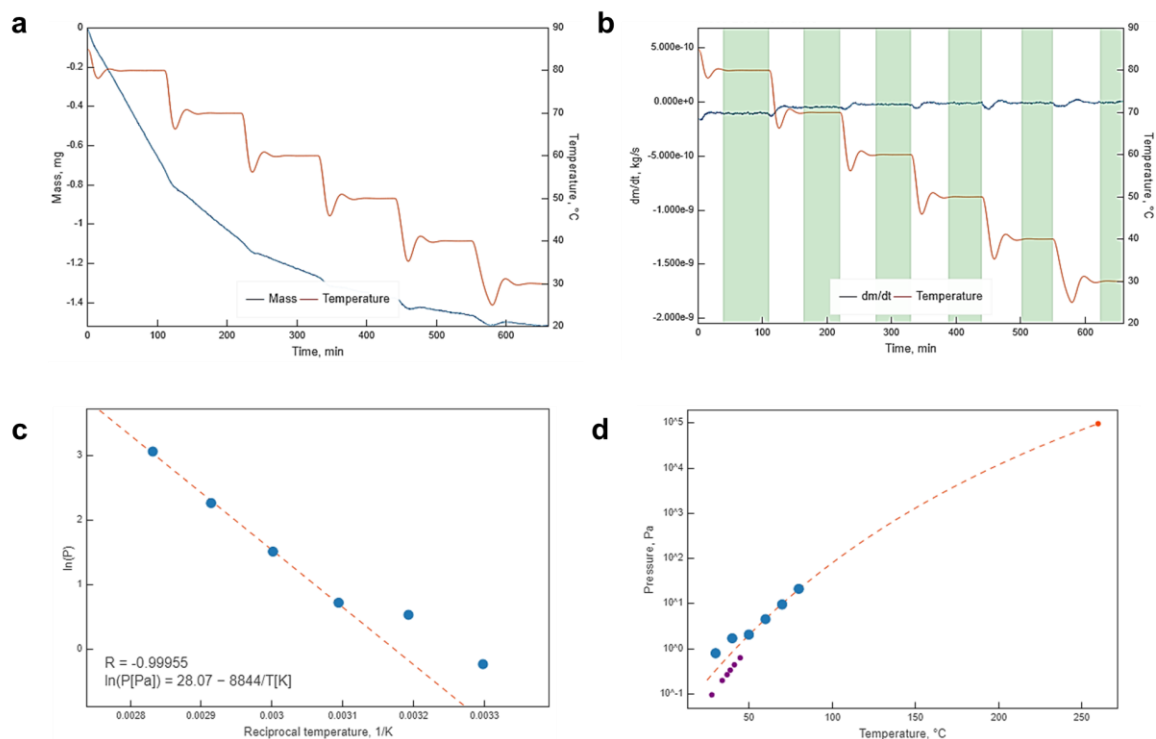
Figure S2 | Vapor pressure determination of 2-methylimidazole. a) Mass loss at different temperature steps as a function of time. **b)** Mass loss derivative at different temperatures as a function of time. The green vertical segments indicate the isothermal steps. **c)** Calculated values with the derived Clausius-Clapeyron plot, and **d)** calculated vapor pressure at the operating temperature range of interest. Experimental data from literature[32] are added (purple dots) showing good agreement with the values obtained in this work.
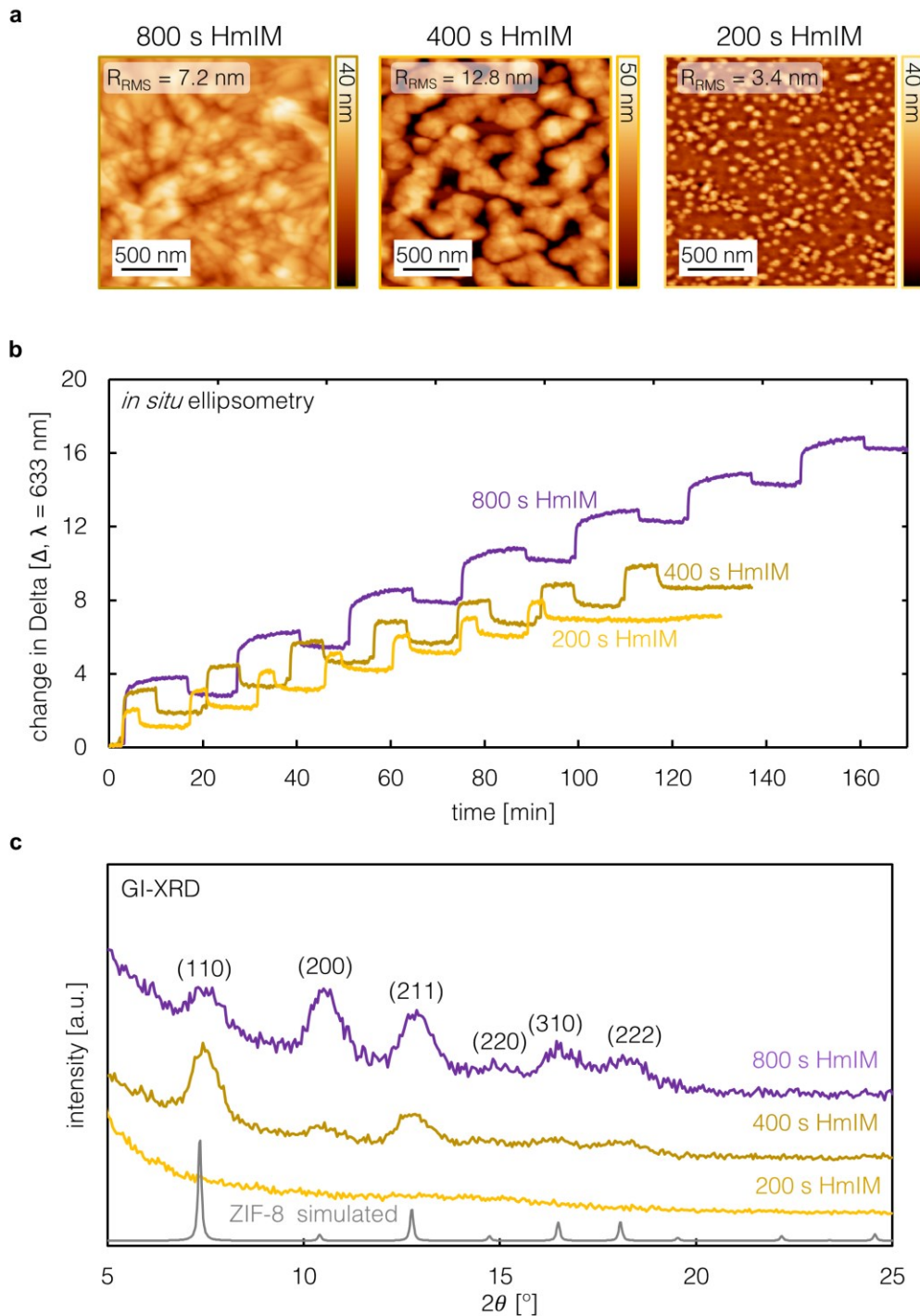
Figure S3 | Direct ZIF-8 MLD linker exposure times. a) AFM images of the MOF-MLD ZIF-8 layer (30 cycles) using different linker (HmIM) exposure times: 800 s (full exposure, purple), 400 s (50% of full exposure, brown), and 200 s (25% of full exposure, yellow) with all other process parameters held constant. **b)** Corresponding *in situ* ellipsometry profiles (change in the ellipsometric parameter, Delta, λ = 633 nm), and **c)** GIXRD of the as-deposited films (including an activated sample for the 50% t_{HmIM} sample). The AFM roughness (R_{RMS}) values are calculated for a 2 × 2 μm^2 probe area.
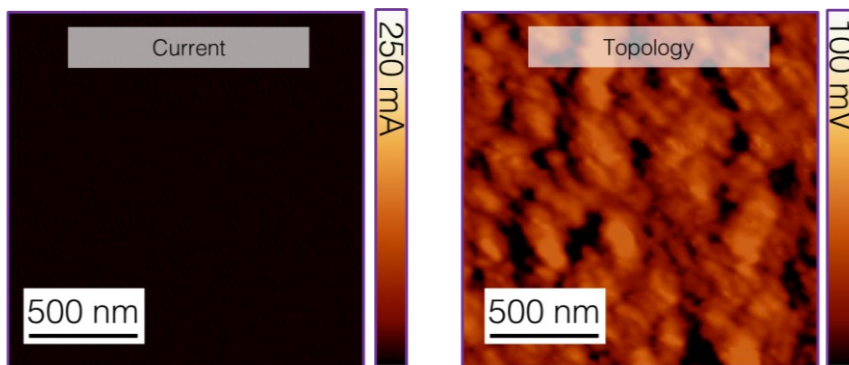
Figure S4 | Direct ZIF-8 MLD films on Si are pinhole-free. Conductive AFM of 10 cycles of direct ZIF-8 MLD.
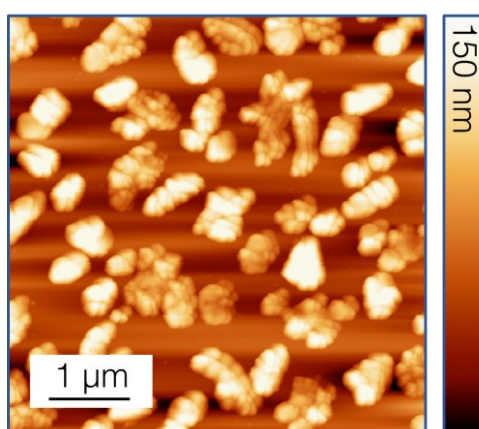

Figure S5 | AFM image of a MOF-CVD ZIF-8 "layer", i.e., scattered crystallites, using 1.8 nm ALD ZnO as the precursor.
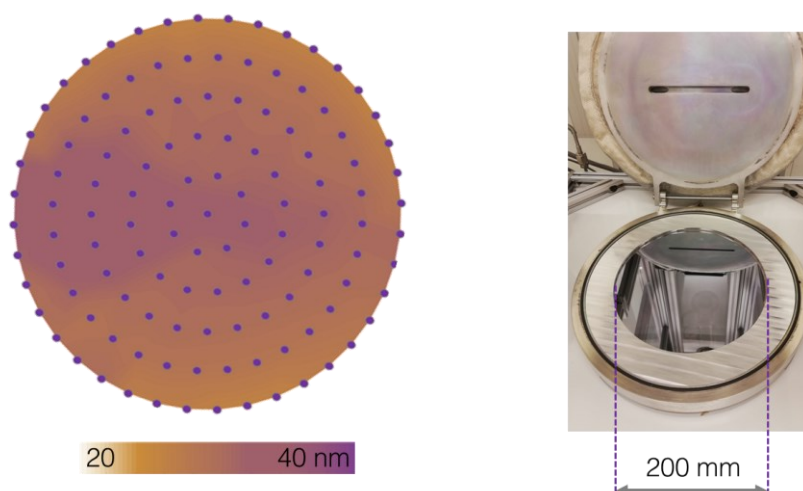

Figure S6 | Photograph of a 200 mm wafer with 30 MLD ZIF-8 cycles and the corresponding 100-point ellipsometry thickness mapping.
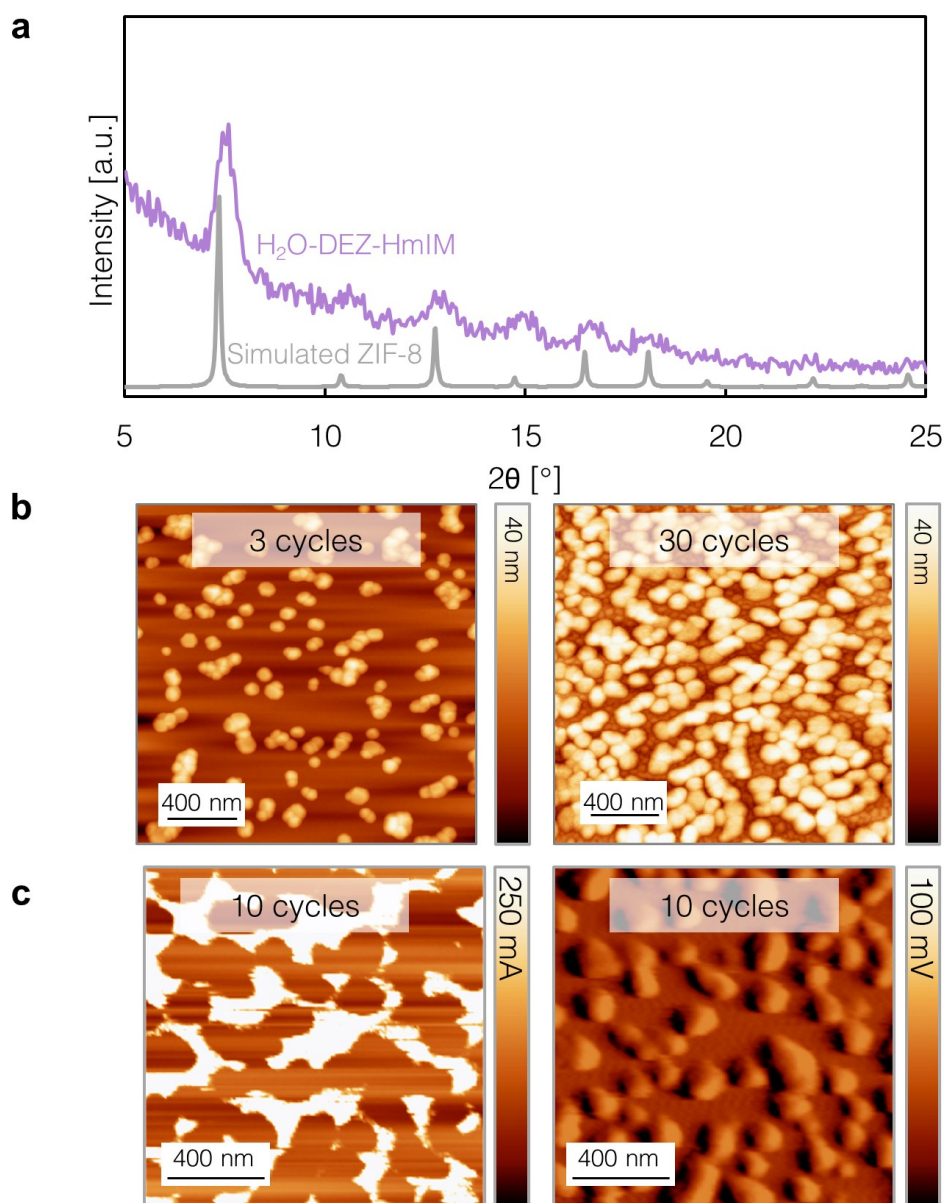
Figure S7 | Film characterization of direct ZIF-8 MLD with a missing water pulse. H_2O-DEZ-HmIM instead of H_2O-DEZ-H_2O-HmIM **a)** GIXRD shows crystalline features, with only the (110) at 7.3° strongly visible. **b)** AFM shows a tendency towards island growth. **c)** c-AFM shows pinholes at 10 cycles of MOF-MLD.
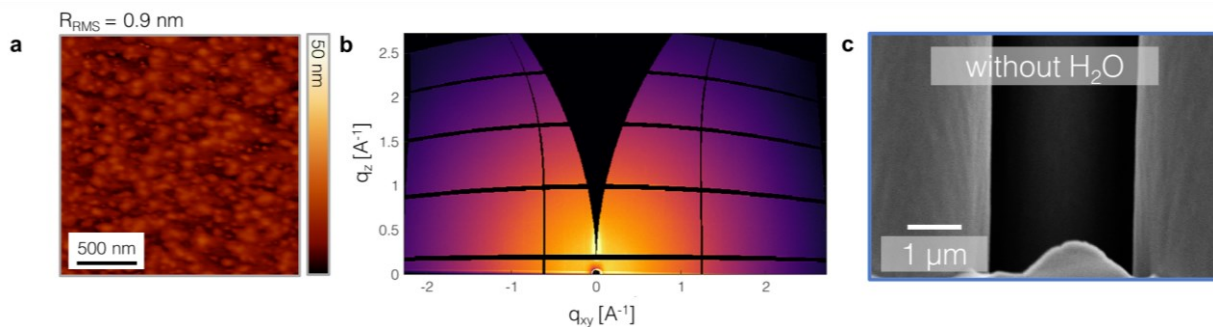
Figure S8 | Effect of no water pulses in direct ZIF-8 MLD. a) AFM image, **b)** synchrotron GIXRD reciprocal space map, and **c)** SEM image of deposition on high-aspect-ratio pillar of direct ZIF-8 MLD without any water included.
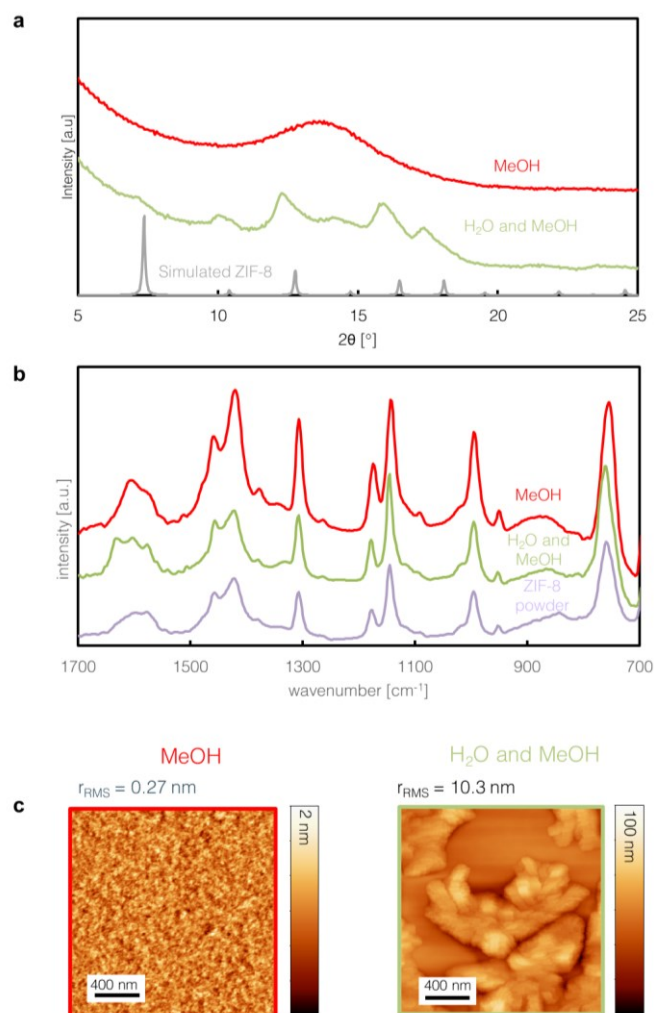

Figure S9 | Direct ZIF-8 MLD (30 cycles) with water entirely or partially substituted by methanol. a) GIXRD pattern, **b)** ATR-FTIR spectra, and **c)** AFM images comparing complete substitution of water with methanol (red), partial substitution (green), and a reference powder (purple).
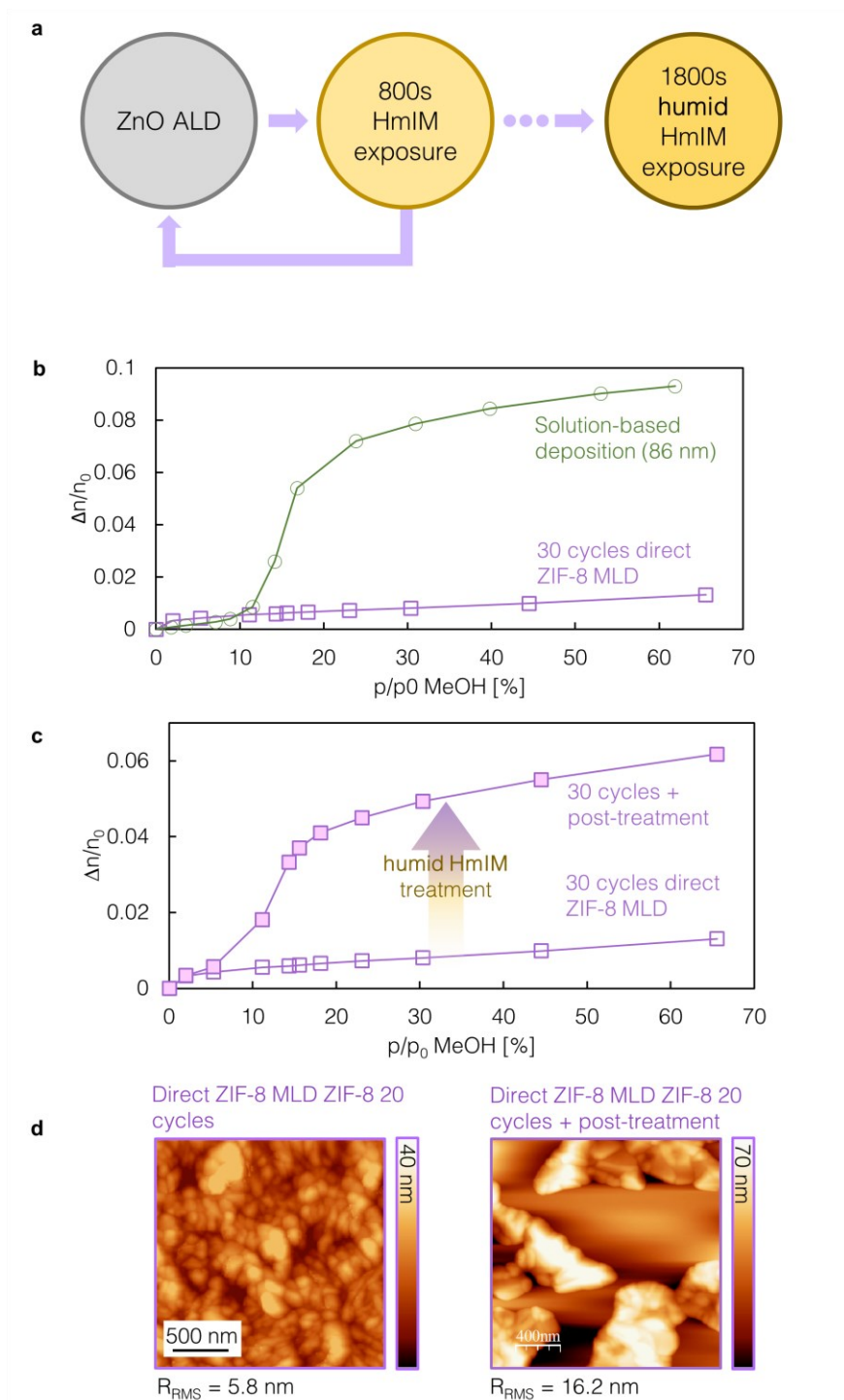
Figure S10 | Humidified conditions HmIM post-deposition treatment of direct ZIF-8 MLD. a) Schematic of direct ZIF-8 MLD followed by humidified conditions post-deposition treatment. **b)** Ellipsometric porosimetry comparing direct ZIF-8 MLD and solution deposited ZIF-8 (deposited according to Lu and Hupp[1]). **c)** Ellipsometric porosimetry, comparison with as-deposited direct ZIF-8 MLD, and humidified conditions HmIM post-treated sample. Both films are modelled with an extended Cauchy model. **d)** Comparison in morphology and coverage of an as-deposited and a post-deposition treated sample.
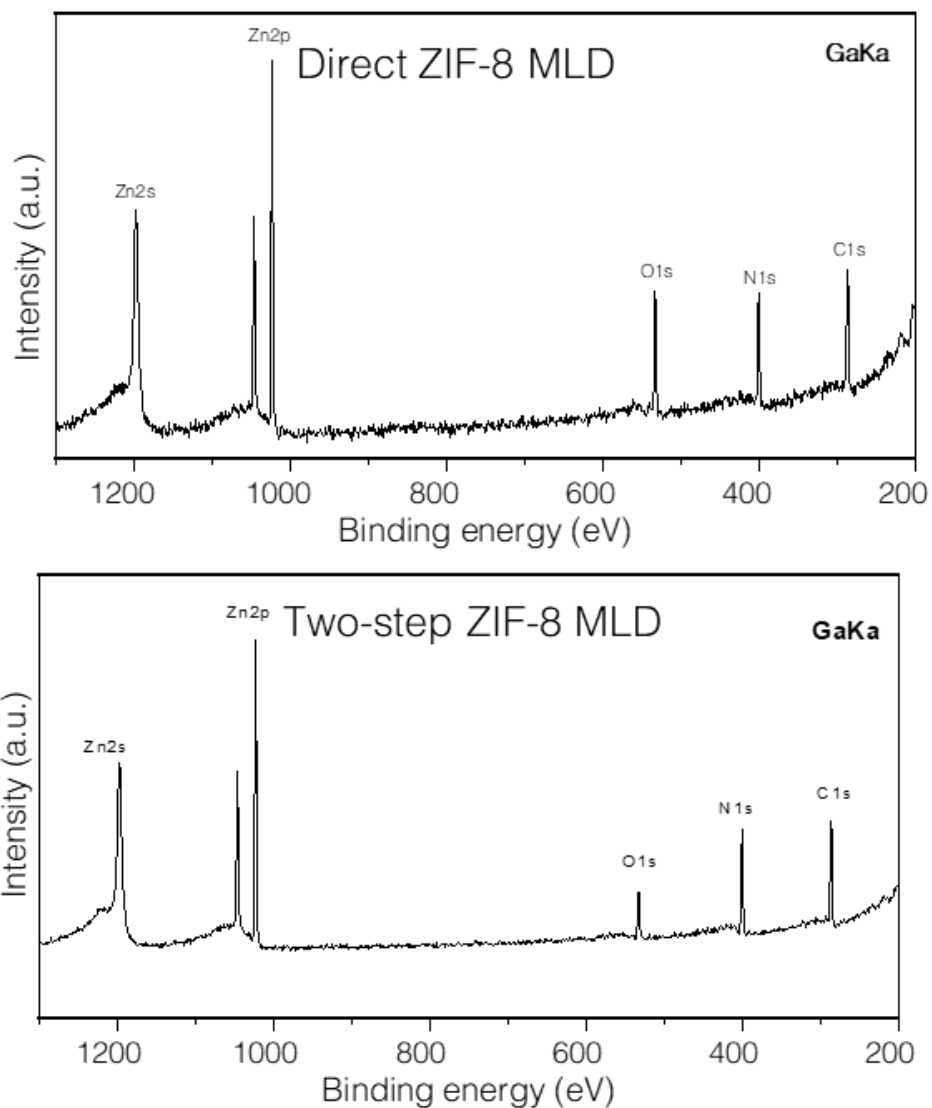
Figure S11 | Hard X-ray photoelectron spectroscopy (HAXPES) survey scans for direct ZIF-8 MLD (top, 10 cycles, ~10 nm) and two-step ZIF-8 MLD (bottom, ~27 nm). Exposure to air was minimized by packaging the samples in nitrogen immediately after deposition for transport to the spectrometer. For direct ZIF-8 MLD an increased oxygen signal is visible. This observation can be attributed to the SiO_2 signal from the native oxide, which is less present for two-step ZIF-8 MLD due to the increased thickness. Furthermore, the increased presence of oxygen can partially be attributed to a higher defect concentration.
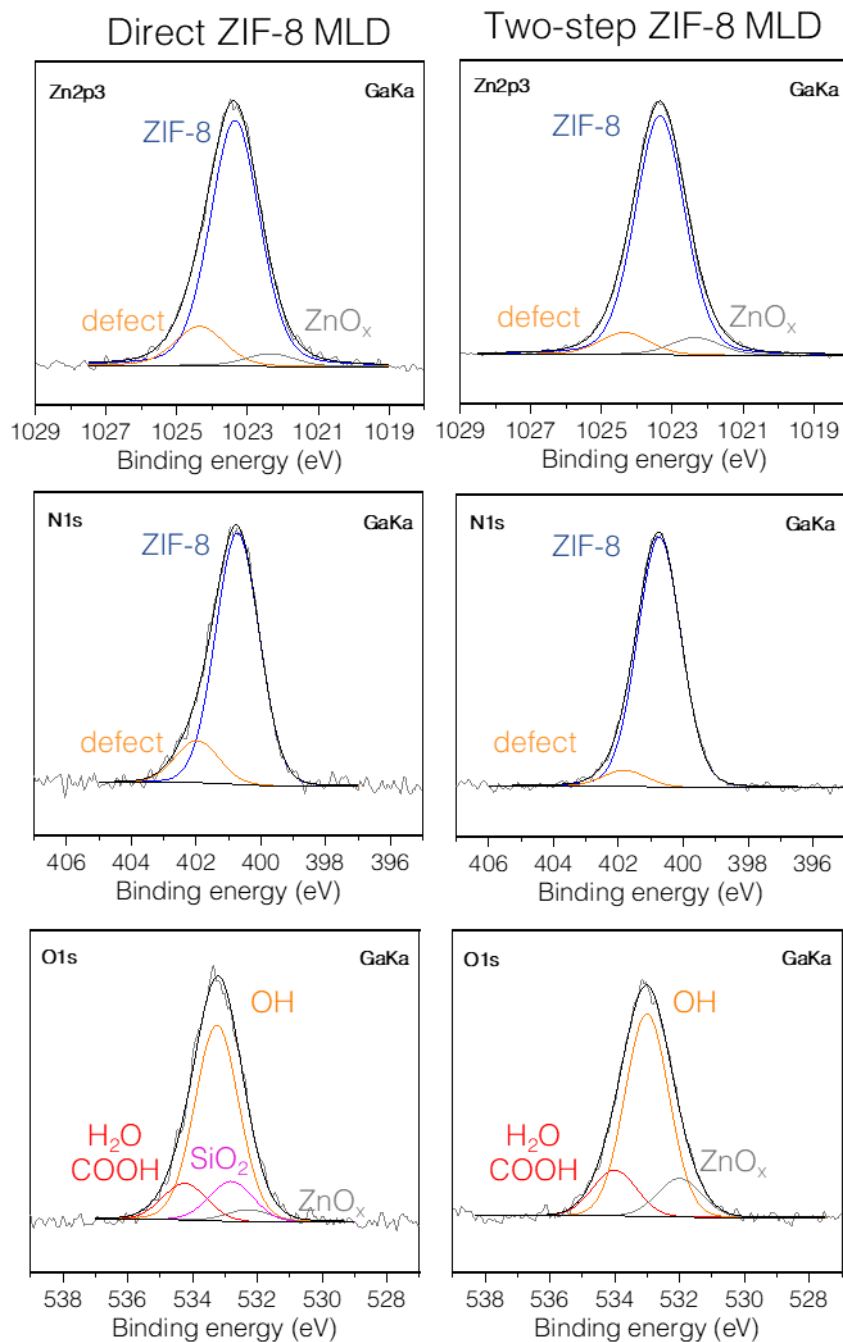
Figure S12 | HAXPES peak fitting for direct ZIF-8 MLD (left, 10 cycles, ~10 nm) and two-step ZIF-8 MLD (right, 30 cycles, ~27 nm). Exposure to air was minimized by packaging the samples in nitrogen immediately after deposition for transport to the spectrometer. For the zinc and nitrogen peaks, subpeaks characteristic of ZIF-8 are shown in blue, and in orange high energy defects peaks are plotted, which cannot be identified since various potential defect peaks are overlapping. A lower intensity of this defect peak is fitted for two-step ZIF-8 MLD. Therefore, these films approach the ideal ZIF-8 structure more closely. In the oxygen peak OH (orange), H_2O or carboxyl (red), ZnOx (grey), and SiO_2 (pink) subpeaks can be fitted.
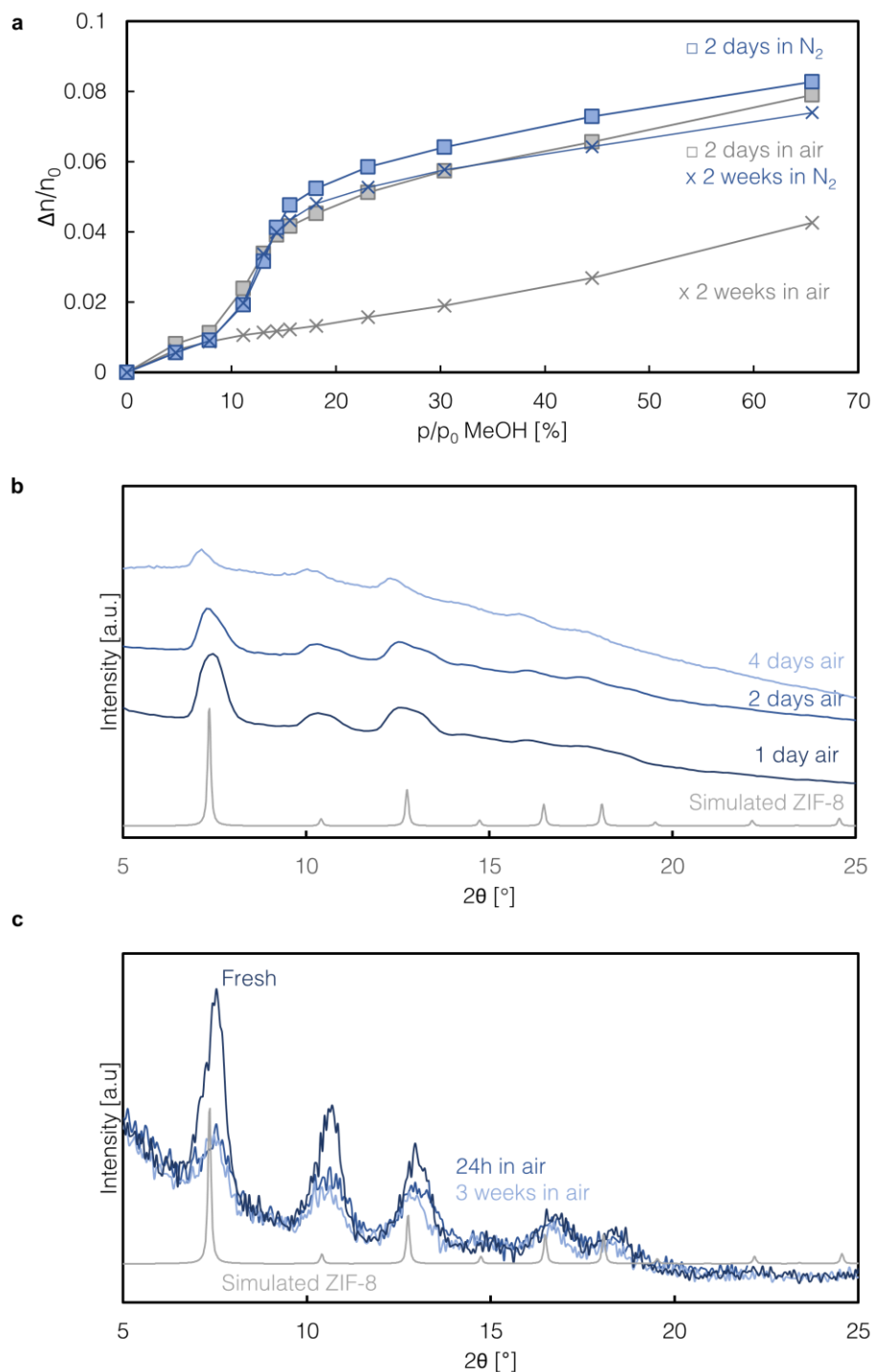
Figure S13 | Study of aging due to exposure to the lab atmosphere with **a)** Ellipsometric porosimetry, all modeled as a Cauchy layer with 10% voids: Decrease in methanol uptake with exposure time to the lab atmosphere. Loss of characteristic S-shaped isotherm at two weeks of air exposure. **b)** Synchrotron GIXRD: decreasing peak intensity with increasing exposure to air. **c)** Lab-based GIXRD: decreasing peak intensity with exposure to air, though at longer exposure times, degradation seems to saturate (*i.e.*, peak intensity stays constant).
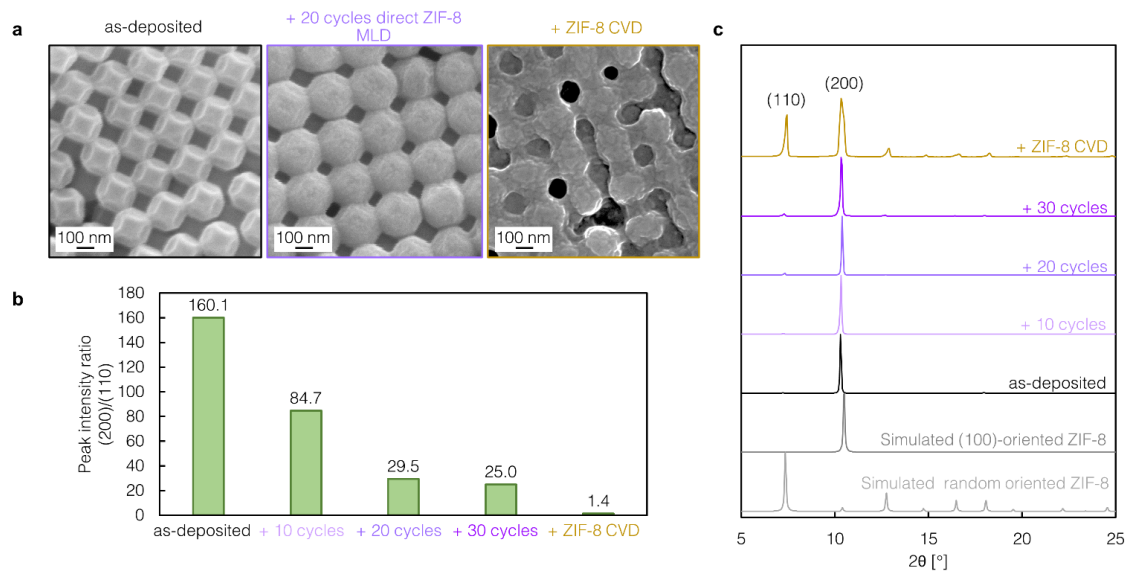
Figure S14 | Direct ZIF-8 MLD on (100) oriented supercrystals. Comparison between bare ZIF-8 supercystals, supercystals coated with direct ZIF-8 MLD (10, 20, and 30 cycles, 9 Å/cycle), and supercrystals coated with ZIF-8 CVD (from 3 nm ZnO, corresponding to ~30 nm of ZIF-8²) a) SEM images b) Peak intensity ratio of (200) peak relative to (110) c) s-XRD patterns normalized to the highest intensity peak.
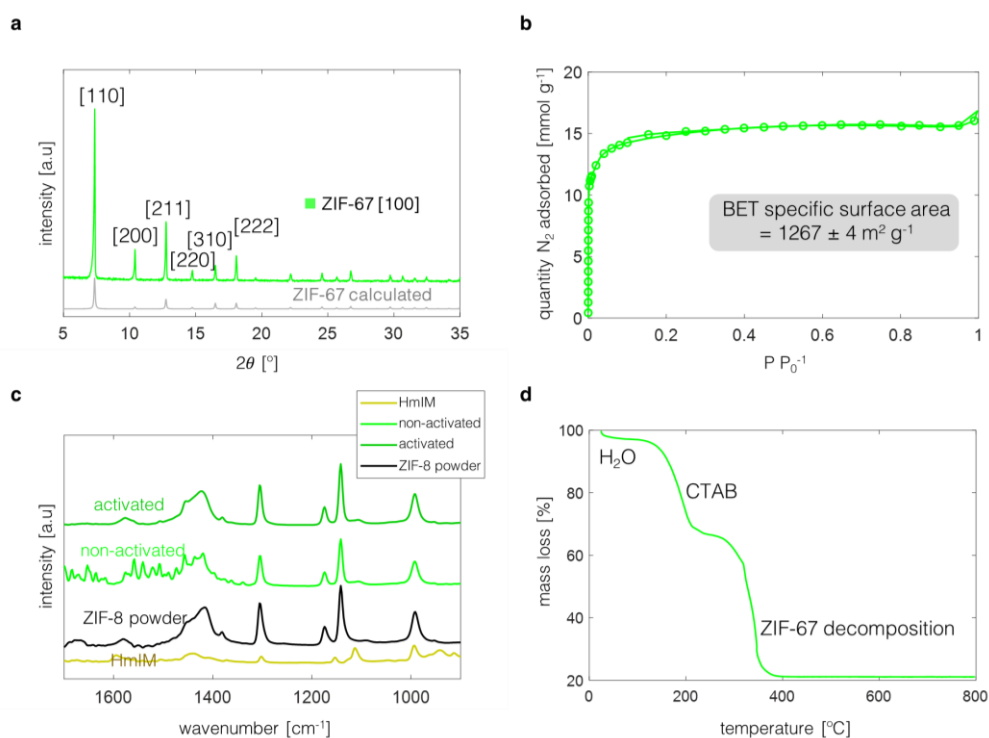

Figure S15 | ZIF-67 crystals powder characterization. a) Powder XRD **b)** N_2 physisorption **c)** ATR-FTIR, and **d)** thermogravimetric analysis of the ZIF-67 crystallites, adapting the method implemented by Avci, *et al*, for ZIF-8.[34] To generate the Co analog of ZIF-8, cobalt acetate [$Co(Ac)_2$ ·4 H_2O] was used as the metal precursor instead of a Zn salt[35] (see *Methods*). The FTIR spectra of ZIF-8 powder generated via solution-based synthesis and HmIM powder are included as references. CCDC code for the calculated ZIF-67 diffraction pattern: GITTOT.[36]
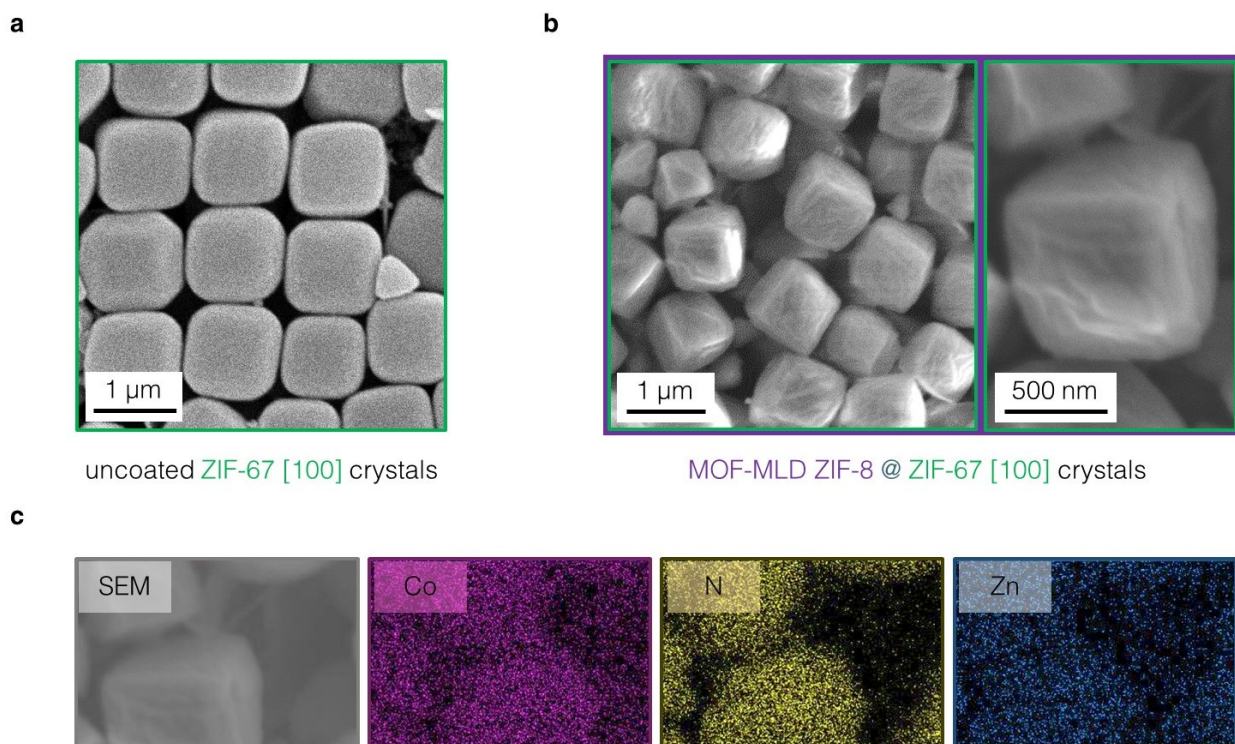
a uncoated ZIF-67 [100] crystals

b MOF-MLD ZIF-8 @ ZIF-67 [100] crystals

c

Figure S16 | SEM images ZIF-67 crystals a) before and **b)** after 20 direct ZIF-8 MLD cycles. **c)** Energy-dispersive X-ray spectroscopy (EDX) shows the conformal ZIF-8 (Zn) coating on ZIF-67 (Co).
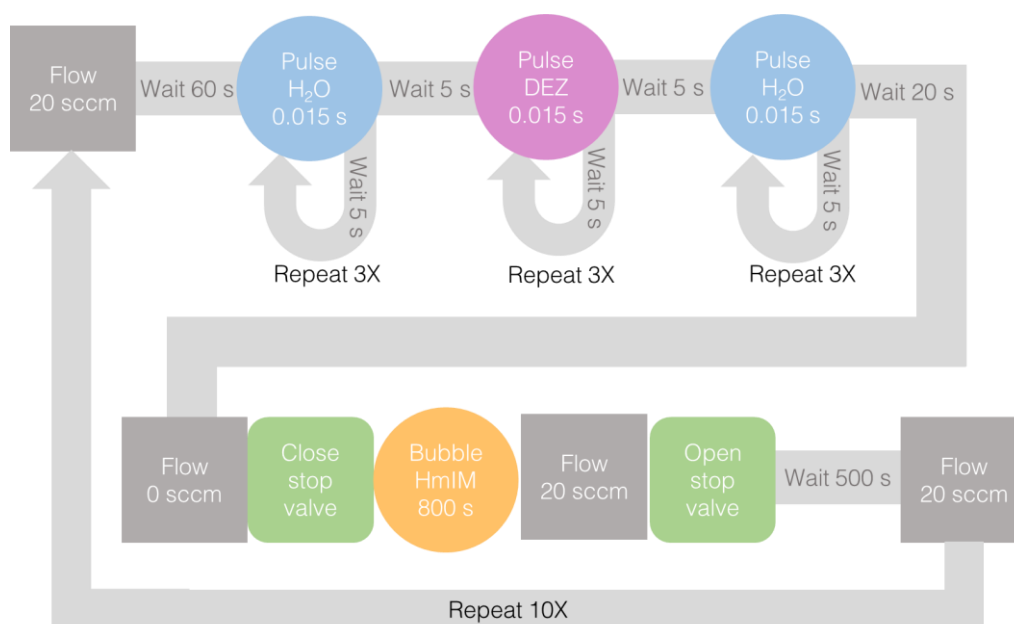

Figure S17 | Direct ZIF-8 MLD schematic representation of the protocol.
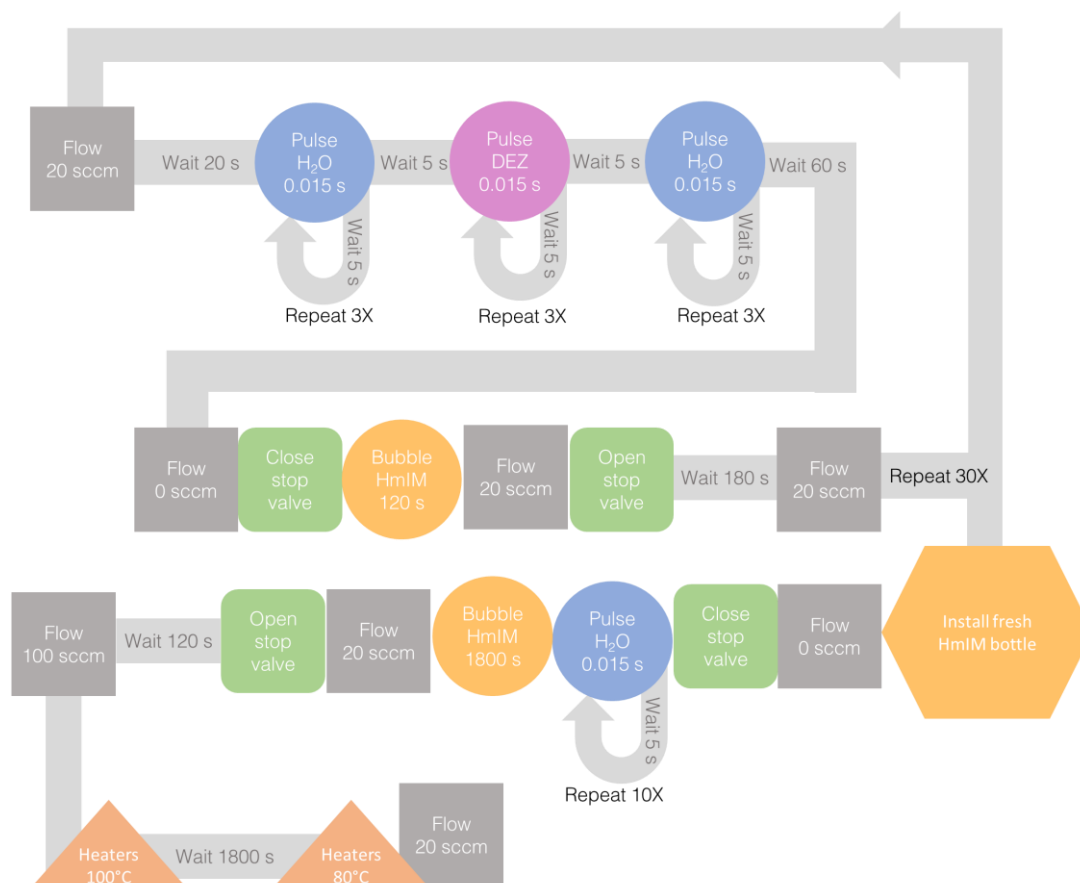
Figure S18 | Two-step ZIF-8 MLD schematic representation of the protocol.

Figure S19 | The optimized temperature gradient in the MOF-MLD reactor. The MOF–MLD chamber has three independently controlled heating zones: the substrate (**1 –** base heater and **2 –** outer ring) and wall (**3 –** lid) heaters. These heaters were set to 80 °C (**1, 2**) and 150 °C (**3**), respectively in MOF-MLD. These are the same optimized temperatures for MOF-CVD detailed in our previous work.[2]

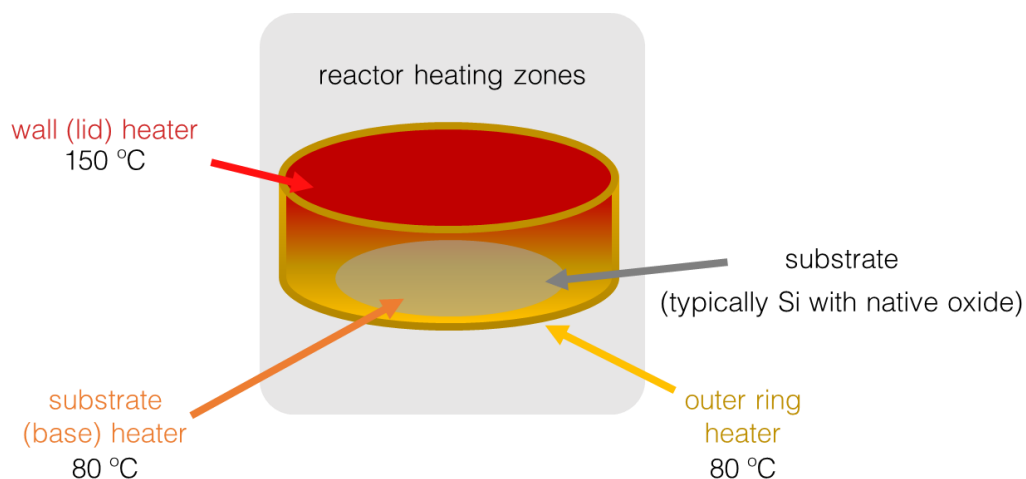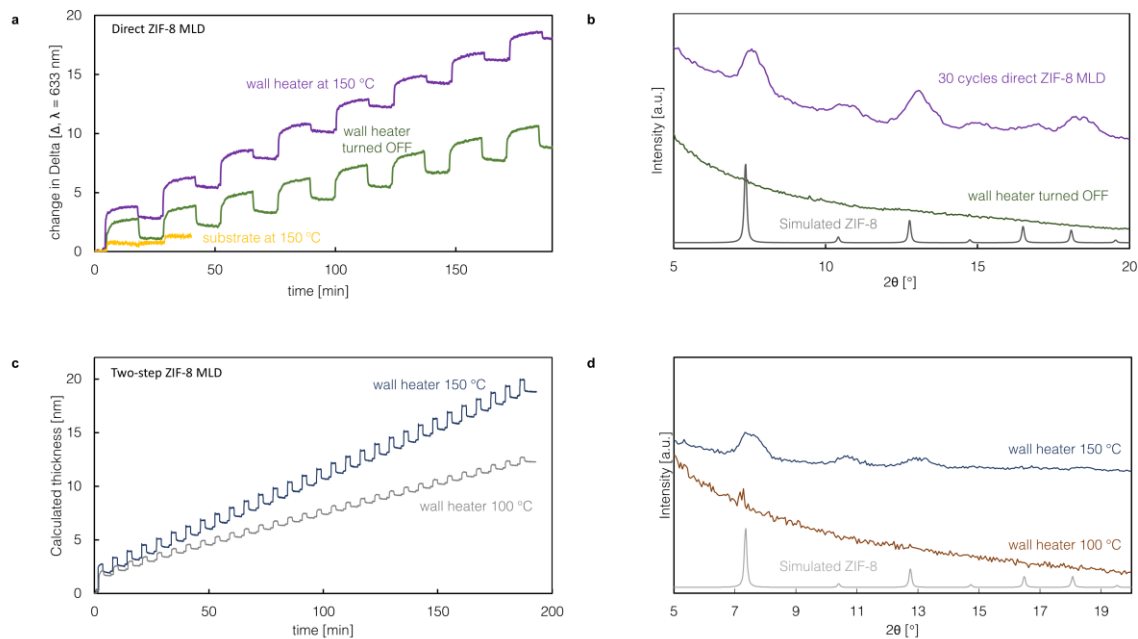**Figure S20 | MOF-MLD optimization of the temperature gradient. a)** *in-situ* ellipsometry profiles (change in Delta, at λ = 633 nm) for direct ZIF-8 MLD (purple); the same MLD recipe with the wall heater turned OFF (green, substrate heater at 80 ˚C), and with the wall and substrate heaters set to 150 °C (2 cycles, yellow), with all other process parameters held constant. **b)** GIXRD patterns of direct ZIF-8 MLD (purple) and a sample deposited with the same protocol but with the wall heater turned off (green). **c)** Modelled *in-situ* ellipsometry of the MLD subsection of two-step ZIF-8 MLD. Comparison between wall heater at 150 °C and at 100°C, *i.e.*, a diminishment of the vertical temperature gradient. **d)** GIXRD pattern comparison between two-step ZIF-8 MLD with wall heater at 150 °C and 100 °C. No significant crystallinity was detected with the wall heater at 100 °C.
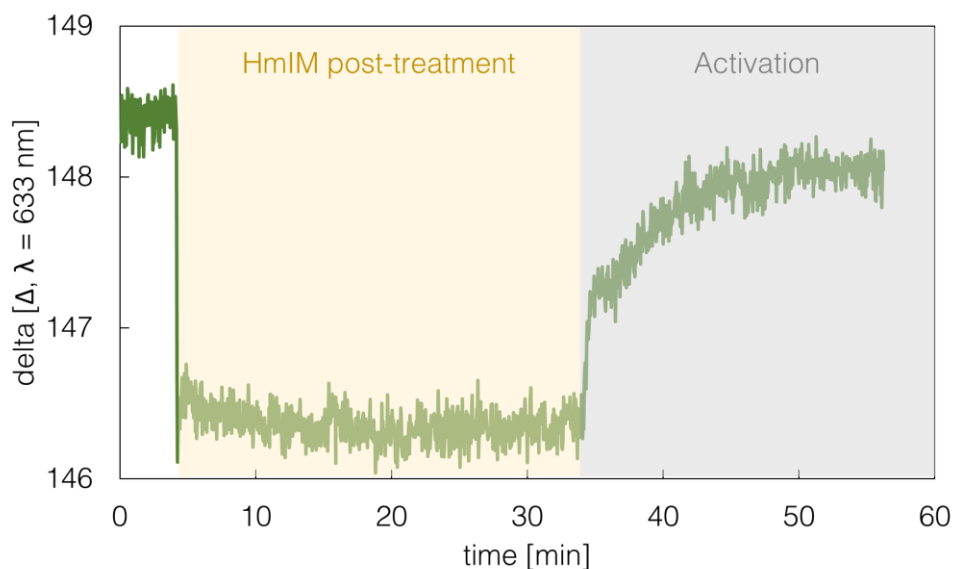
Figure S21 | Ellipsometry of HmIM post-deposition treatment and activation in two-step ZIF-8 MLD. Delta at 633 nm as a function of time.
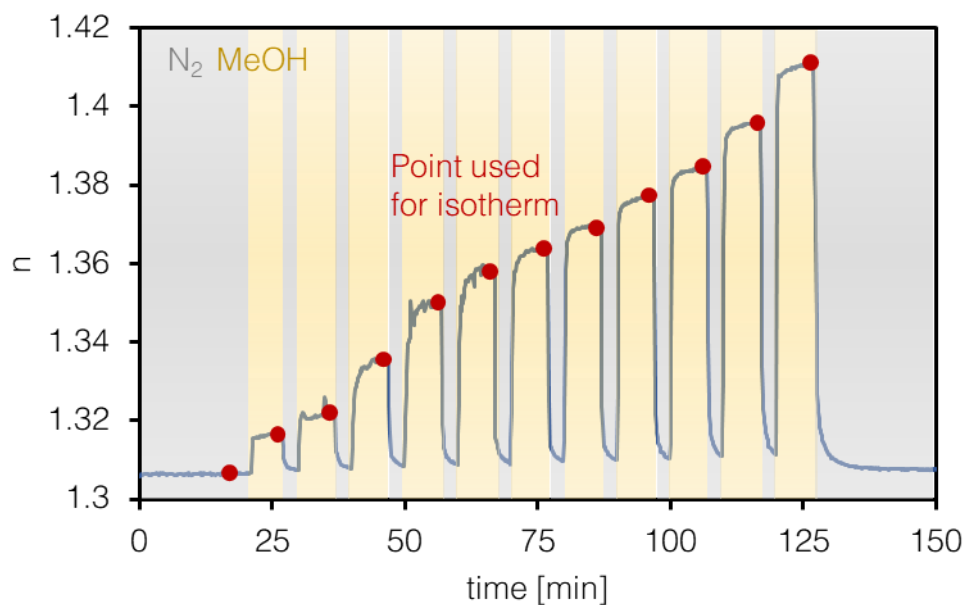
Figure S22 | Ellipsometric porosimetry as a function of time. Two-step ZIF-8 MLD film on Si, where the sample is exposed to eleven different MeOH vapor concentrations separated by inert gas purge streams. Grey areas indicate N_2 purge times, yellow methanol vapor exposure, and red dots indicate the points at which data for the isotherms is exported.

Supporting Information References

(1) Lu, G.; Hupp, J. T. Metal–Organic Frameworks as Sensors: A ZIF-8 Based Fabry–Pérot Device as a Selective Sensor for Chemical Vapors and Gases. *J. Am. Chem. Soc.* **2010**, *132* (23), 7832–7833. https://doi.org/10.1021/ja101415b.

(2) Cruz, A. J.; Stassen, I.; Krishtab, M.; Marcoen, K.; Stassin, T.; Rodríguez-Hermida, S.; Teyssandier, J.; Pletincx, S.; Verbeke, R.; Rubio-Giménez, V.; Tatay, S.; Martí-Gastaldo, C.; Meersschaut, J.; Vereecken, P. M.; De Feyter, S.; Hauffman, T.; Ameloot, R. Integrated Cleanroom Process for the Vapor-Phase Deposition of Large-Area Zeolitic Imidazolate Framework Thin Films. *Chem. Mater.* **2019**, *31* (22), 9462–9471. https://doi.org/10.1021/acs.chemmater.9b03435.

(3) Heinke, L. Diffusion and Photoswitching in Nanoporous Thin Films of Metal-Organic Frameworks. *J. Phys. Appl. Phys.* **2017**, *50* (19), 193004. https://doi.org/10.1088/1361-6463/aa65f8.

(4) Chmelik, C.; Bux, H.; Caro, J.; Heinke, L.; Hibbe, F.; Titze, T.; Kärger, J. Mass Transfer in a Nanoscale Material Enhanced by an Opposing Flux. *Phys. Rev. Lett.* **2010**, *104* (8), 085902. https://doi.org/10.1103/PhysRevLett.104.085902.

(5) Tompkins, H. G.; Hilfiker, J. N. *Spectroscopic Ellipsometry: Practical Application to Thin Film Characterization*; Materials characterization and analysis collection; Momentum Press: New York, NY, 2016.

(6) Horcas, I.; Fernández, R.; Gómez-Rodríguez, J. M.; Colchero, J.; Gómez-Herrero, J.; Baro, A. M. WSXM: A Software for Scanning Probe Microscopy and a Tool for Nanotechnology. *Rev. Sci. Instrum.* **2007**, *78* (1), 013705. https://doi.org/10.1063/1.2432410.

(7) Krywka, C.; Paulus, M.; Sternemann, C.; Volmer, M.; Remhof, A.; Nowak, G.; Nefedov, A.; Pöter, B.; Spiegel, M.; Tolan, M. The New Diffractometer for Surface X-Ray Diffraction at Beamline BL9 of DELTA. *J. Synchrotron Radiat.* **2006**, *13* (1), 8–13. https://doi.org/10.1107/S0909049505035685.

(8) Hammersley, A. P.; Svensson, S. O.; Hanfland, M.; Fitch, A. N.; Hausermann, D. Two-Dimensional Detector Software: From Real Detector to Idealised Image or Two-Theta Scan. *High Press. Res.* **1996**, *14* (4–6), 235–248. https://doi.org/10.1080/08957959608201408.

(9) B, S.; S, P.; M, D.; C, R.; J, D.; T, F.; R, R.; O, W. GIDVis: A Comprehensive Software Tool for Geometry-Independent Grazing-Incidence X-Ray Diffraction Data Analysis and Pole-Figure Calculations. *J. Appl. Crystallogr.* **2019**, *52* (3), 683–689. https://doi.org/10.1107/S1600576719004485.

(10) Tietze, M. L.; Obst, M.; Arnauts, G.; Wauteraerts, N.; Rodríguez-Hermida, S.; Ameloot, R. Parts-per-Million Detection of Volatile Organic Compounds via Surface Plasmon Polaritons and Nanometer-Thick Metal–Organic Framework Films. *ACS Appl. Nano Mater.* **2022**, acsanm.2c00012. https://doi.org/10.1021/acsanm.2c00012.

(11) Trzhaskovskaya, M. B.; Yarzhemsky, V. G. Dirac–Fock Photoionization Parameters for HAXPES Applications. *At. Data Nucl. Data Tables* **2018**, *119*, 99–174. https://doi.org/10.1016/j.adt.2017.04.003.

(12) Avci, C.; Liu, Y.; Pariente, J. A.; Blanco, A.; Lopez, C.; Imaz, I.; Maspoch, D. Template-Free, Surfactant-Mediated Orientation of Self-Assembled Supercrystals of Metal–Organic Framework Particles. *Small* **2019**, *15* (31), 1902520. https://doi.org/10.1002/smll.201902520.

(13) Chen, X.; Oja, V.; Chan, W. G.; Hajaligol, M. R. Vapor Pressure Characterization of Several Phenolics and Polyhydric Compounds by Knudsen Effusion Method. *J. Chem. Eng. Data* **2006**, *51* (2), 386–391. https://doi.org/10.1021/je050293h.

(14) Salmi, L.; Heikkilä, M.; Puukilainen, E.; Sajavaara, T.; Grosso, D.; Ritala, M. Studies on Atomic Layer Deposition of MOF-5 Thin Films. *Microporous Mesoporous Mater.* **2013**, *182*, 147–154. https://doi.org/10.1016/j.micromeso.2013.08.024.

(15)   Salmi, L. D.; Heikkilä, M. J.; Vehkamäki, M.; Puukilainen, E.; Ritala, M.; Sajavaara, T. Studies on Atomic Layer Deposition of IRMOF-8 Thin Films. *J. Vac. Sci. Technol. A* **2014**, 33 (1), 01A121. https://doi.org/10.1116/1.4901455.

(16)   Ahvenniemi, E.; Karppinen, M. Atomic/Molecular Layer Deposition: A Direct Gas-Phase Route to Crystalline Metal–Organic Framework Thin Films. *Chem. Commun.* **2016**, 52 (6), 1139–1142. https://doi.org/10.1039/C5CC08538A.

(17)   Multia, J.; Kravchenko, D. E.; Rubio-Giménez, V.; Philip, A.; Ameloot, R.; Karppinen, M. Nanoporous Metal–Organic Framework Thin Films Prepared Directly from Gaseous Precursors by Atomic and Molecular Layer Deposition: Implications for Microelectronics. *ACS Appl. Nano Mater.* **2023**, 6 (2), 827–831. https://doi.org/10.1021/acsanm.2c04934.

(18)   Medishetty, R.; Zhang, Z.; Sadlo, A.; Cwik, S.; Peeters, D.; Henke, S.; Mangayarkarasi, N.; Devi, A. Fabrication of Zinc-Dicarboxylate- and Zinc-Pyrazolate-Carboxylate-Framework Thin Films through Vapour-Solid Deposition. *Dalton Trans.* **2018**, 47 (40), 14179–14183. https://doi.org/10.1039/C8DT00352A.

(19)   Ahvenniemi, E.; Karppinen, M. In Situ Atomic/Molecular Layer-by-Layer Deposition of Inorganic–Organic Coordination Network Thin Films from Gaseous Precursors. *Chem. Mater.* **2016**, 28 (17), 6260–6265. https://doi.org/10.1021/acs.chemmater.6b02496.

(20)   Lausund, K. B.; Nilsen, O. All-Gas-Phase Synthesis of UiO-66 through Modulated Atomic Layer Deposition. *Nat. Commun.* **2016**, 7 (1). https://doi.org/10.1038/ncomms13578.

(21)   Lausund, K. B.; Petrovic, V.; Nilsen, O. All-Gas-Phase Synthesis of Amino-Functionalized UiO-66 Thin Films. *Dalton Trans.* **2017**, 46 (48), 16983–16992. https://doi.org/10.1039/C7DT03518G.

(22)   Lausund, K. B.; Olsen, M. S.; Hansen, P.-A.; Valen, H.; Nilsen, O. MOF Thin Films with Bi-Aromatic Linkers Grown by Molecular Layer Deposition. *J. Mater. Chem. A* **2020**, 8 (5), 2539–2548. https://doi.org/10.1039/C9TA09303F.

(23)   Tanskanen, A.; Karppinen, M. Iron-Terephthalate Coordination Network Thin Films Through In-Situ Atomic/Molecular Layer Deposition. *Sci. Rep.* **2018**, 8 (1), 8976. https://doi.org/10.1038/s41598-018-27124-7.

(24)   Han, S.; Ciufo, R. A.; Meyerson, M. L.; Keitz, B. K.; Mullins, C. B. Solvent-Free Vacuum Growth of Oriented HKUST-1 Thin Films. *J. Mater. Chem. A* **2019**, 7 (33), 19396–19406. https://doi.org/10.1039/C9TA05179A.

(25)   Khayyami, A.; Philip, A.; Karppinen, M. Atomic/Molecular Layer Deposited Iron–Azobenzene Framework Thin Films for Stimuli-Induced Gas Molecule Capture/Release. *Angew. Chem. Int. Ed.* **2019**, 58 (38), 13400–13404. https://doi.org/10.1002/anie.201908164.

(26)   Silva, R. M.; Carlos, L. D.; Rocha, J.; Silva, R. F. Luminescent Thin Films of Eu-Bearing UiO-66 Metal Organic Framework Prepared by ALD/MLD. *Appl. Surf. Sci.* **2020**, 527, 146603. https://doi.org/10.1016/j.apsusc.2020.146603.

(27)   Yase, K.; Takahashi, Y.; Ara-kato, N.; Kawazu, A. Evaporation Rate and Saturated Vapor Pressure of Functional Organic Materials. *Jpn. J. Appl. Phys.* **1995**, 34 (2R), 636. https://doi.org/10.1143/JJAP.34.636.

(28)   Wakayama, N.; Inokuchi, H. Heats of Sublimation of Polycyclic Aromatic Hydrocarbons and Their Molecular Packings. *Bull. Chem. Soc. Jpn.* **1967**, 40 (10), 2267–2271. https://doi.org/10.1246/bcsj.40.2267.

(29)   Niskanen, A.; Hatanpää, T.; Ritala, M.; Leskelä, M. Thermogravimetric Study of Volatile Precursors For Chemical Thin Film Deposition. Estimation of Vapor Pressures and Source Temperatures. *J. Therm. Anal. Calorim.* **2001**, 64 (3), 955–964. https://doi.org/10.1023/A:1011579114687.

(30)   Ribeiro da Silva, M. A. V.; Monte, M. J. S.; Santos, L. M. N. B. F. The Design, Construction, and Testing of a New Knudsen Effusion Apparatus. *J. Chem. Thermodyn.* **2006**, 38 (6), 778–787. https://doi.org/10.1016/j.jct.2005.08.013.

(31)   *Handbook of Thermal Analysis and Calorimetry: Recent Advances, Techniques and Applications*; Elsevier: Amsterdam, The Netherlands, 2018.

(32)   Jiménez, P.; Roux, M. V.; Turrión, C. Thermochemical Properties of N-Heterocyclic Compounds IV. Enthalpies of Combustion, Vapour Pressures and Enthalpies of Sublimation, and Enthalpies of Formation of 2-Methylimidazole and 2-Ethylimidazole. *J. Chem. Thermodyn.* **1992**, 24 (11), 1145–1149. https://doi.org/10.1016/S0021-9614(05)80237-X.

(33)   Almeida, A. R. R. P.; Monte, M. J. S. Thermodynamic Study of Phase Transitions of Imidazoles and 1-Methylimidazoles. *J. Chem. Thermodyn.* **2012**, 44 (1), 163–168. https://doi.org/10.1016/j.jct.2011.08.017.

(34)   Avci, C.; Liu, Y.; Pariente, J. A.; Blanco, A.; Lopez, C.; Imaz, I.; Maspoch, D. Template-Free, Surfactant-Mediated Orientation of Self-Assembled Supercrystals of Metal–Organic Framework Particles. *Small* **2019**, 15 (31), 1902520. https://doi.org/10.1002/smll.201902520.

(35)   Qian, J.; Sun, F.; Qin, L. Hydrothermal Synthesis of Zeolitic Imidazolate Framework-67 (ZIF-67) Nanocrystals. *Mater. Lett.* **2012**, 82, 220–223. https://doi.org/10.1016/j.matlet.2012.05.077.

(36)   Banerjee, R.; Phan, Anh; Wang, Bo; Knobler, C.; Furukawa, H.; O'Keeffe, M.; Yaghi, O.M. CCDC 671073: Experimental Crystal Structure Determination, 2008. https://doi.org/10.5517/CCQJ9J1.